Science Bulletin 64 (2019) 1634–1642

Contents lists available at ScienceDirect

Science Bulletin

journal homepage: www.elsevier.com/locate/scib

Article

A new dual-ion battery based on amorphous carbon

Wei (Alex) Wang [a], Hanxin Huang [a], Bin Wang [a], Chang Qian [a], Peihao Li [a], Jinhui Zhou [a], Zibin Liang [a], Chao Yang [a], Shaojun Guo [a,b,c,d,*]

[a] Department of Materials Science and Engineering, College of Engineering, Peking University, Beijing 100871, China
[b] BIC-ESAT, College of Engineering, Peking University, Beijing 100871, China
[c] Beijing Key Laboratory for Magnetoeletric Materials and Devices (BKL-MEMD), Peking University, Beijing 100871, China
[d] Department of Energy and Resources Engineering, College of Engineering, Peking University, Beijing 100871, China

ARTICLE INFO

Article history:
Received 8 June 2019
Received in revised form 19 July 2019
Accepted 2 August 2019
Available online 22 August 2019

Keywords:
Na-based dual-ion batteries
Amorphous carbon
Storage mechanism
Larger interlayer spacing

ABSTRACT

The Na-based dual-ion batteries (NDIBs), combining the advantages of Na-ion batteries and dual-ion batteries, are attracting more attention due to their merits of abundant source, low cost and high energy density. However, the main challenges faced by NDIBs are their low capacity and poor cycling. Herein, we report a new ion storage mechanism for high-performance NDIBs using amorphous carbon (AOMC) as cathode. Unlike the graphite carbon that can only accommodate the PF_6^- anion (typical DIB system), the AOMC herein can both accommodate Na^+ cation and PF_6^- anion due to its amorphous feature, which is conceptually new dual-ion system for achieving much higher capacity. *Ex-situ* X-ray photoelectron spectroscopy, X-ray diffraction and Raman studies reveal that the disordered carbon in the AOMC can be transformed to the partial graphitic stacking in short range, improving both capacity and cycling stability of NDIBs. As a consequence, the AOMC delivers a highly reversible storage capacity of 136 mAh g^{-1} for 800 cycles at a very high current density of 2.0 A g^{-1}, much higher than all the reported NDIBs. Such concept can be generalized to develop high-performance dual-ion full cell using sodium ion pre-intercalated materials as anode and AOMC as cathode.

1. Introduction

Portable electronics and electric vehicles with high energy density and power density are urgently needed due to the rapid growth of the environmental pollution, global population and urbanization and the consumption of traditional fossil sources [1–3]. Lithium-ion batteries (LIBs), as the dominant energy storage devices, have been commercially used since 1990s [4–6]. Despite of the great progress in LIBs industry, the drawbacks are still obvious, such as limited lithium resources and safety issues caused by lithium dendrites, hindering their large-scale applications [7–9]. Designing new battery system is attracting more attention, such as sodium-ion batteries (SIBs) [10,11], potassium-ion batteries (KIBs) [12,13], lithium-air batteries [14,15] and dual-ion batteries (DIBs) [16–18]. The SIBs are considered as promising alternatives to LIBs for energy storage because of their infinite sodium resources. But the main problems faced by SIBs are their low full-cell voltage (Na/Na^+ (−2.71 V vs. standard hydrogen electrode) with 0.3 V higher than Li/Li^+ (−3.04 V)), sluggish kinetics and poor cycling stability [9,19–21]. A Na-based rechargeable battery system with high voltage, high rate and long cycle life is urgently required.

Due to the advantages of high voltage plateau, eco-friendliness, low cost and good safety, the DIBs systems are showing promising prospect superior to LIBs [22,23]. Typically, in the charge process of DIBs, the anion (PF_6^-, $TFSI^-$, etc.) and the cation (Li^+ or Na^+) simultaneously intercalate into or deposit onto the (cathode and anode) materials, respectively, whereas in the discharge process, the anion and cation deintercalate from the electrode and go back to the electrolyte. The layered graphite is composed of a number of graphene layers stacked together by the van der Waals force, which is a common cathode for DIBs. Meantime, the mesocarbon microbead [24], hydrocarbon [25], diamino–rubicene [26] and the layered aromatic amine [27] also have the ability to store the anions. Recent advances in Na-based DIBs (NDIBs) reveal that battery performance can be further enhanced by combining both the advantages of SIBs and DIBs [28,29]. However, the capacity of reported graphite-based NDIBs can only reach 74 mAh g^{-1}, leading to the low energy density in spite of high voltage plateau. Another noticeable issue is that the intercalation/deintercalation of the large size anions into/from the graphite layer can result in large interlayer spacing increasing and huge volume expansion, leading

* Corresponding author.
E-mail address: guosj@pku.edu.cn (S. Guo).

https://doi.org/10.1016/j.scib.2019.08.021
2095-9273/

to poor cycling stability. Other carbonaceous materials, such as the mesocarbon microbead film and pine-needles-derived carbon, were also investigated as NDIB cathodes. However, due to the sluggish kinetics and large radius of cations and anions, neither the capacity nor the cycling stability was satisfactory [30,31]. In this regard, exploring a new intercalation and deintercalation mechanism beyond the existing theory for DIBs is highly desiable for further boosting the capacity, rate ability and stability of battery, yet still a grand challenge.

Herein, we demonstrate a new sodium-based dual ion storage mechanism for boosting the performance of NDIBs in terms of capacity, rate ability and stability by the use of amorphous ordered mesoporous carbon (AOMC) as cathode. It is amizingly found that the AOMC has the ability to accommodate both the PF_6^- anion and Na ion during charge or discharge process whereas only the PF_6^- anions can intercalate into the graphite cathode in transitional NDIBs. Another noticeable feature is that although the original AOMC is amorphous, while after cycling, the disordered carbon is transformed to the partial graphitic stacking in short range. The large interlayer spacing (4.36 Å, much larger than that of graphite) and the unique layered structure in short range can accommodate more ions into the carbon layer and tolerate the increase of the interlayer spacing and the volume expansion. These make AOMC-based new NDIBs system exhibit much higher capacity, higher rate ability and longer cycling than graphene-based traditional NDIBs system. This new discovery is also performed in full-cell NDIBs using sodium ion pre-intercalated materials as anode and AOMC as cathode, which not only highlights the importance of introducing AOMC as an ideal cathode for high-performance NDIBs but also provides a new thought on the design of rechargeable multi-ion batteries in the future.

2. Experimental

2.1. Synthesis of the graphene grown on the nickle foam (GNF)

The GNF was synthesized through a chemical vapor deposition (CVD) method [32,33]. The nickel foam was washed by ultrapure water, acetone and ethanol for 30 min, respectively under ultrasonication. The nickel foam was dried under vacuum for 1 h. Then the nickel foam was loaded into a CVD chamber and heated at 1000 °C for 20 min under the mixed gases of H_2 (10%) and Ar (90%), respectively. Then the above mixed gases were turned off, and the CVD process was carried out at 1000 °C for 30 min under CH_4 atmosphere. When the CVD process was finished, the CH_4 gas was turned off and the N_2 gas was turned on till the CVD chamber was cooled down to room temperature.

2.2. Synthesis of the amorphous ordered mesoporous carbon (AOMC)

SBA-15 silica template was synthesized according to the previous reports [34,35]. 2.0 g of the SBA-15 was added into a solution containing 2.5 g of sucrose and 0.28 g of H_2SO_4 in 10 mL distilled water. Then the mixture was firstly dried at 100 °C for 6 h and continued to dry at 160 °C for 6 h in an oven. The above product was added into a solution containing 1.6 g of sucrose and 0.18 g of H_2SO_4 in 10 mL distilled water. The obtained product was carbonized by pyrolysis at 900 °C under vacuum. Then 5 wt% of hydrofluoric acid was used to remove the silica template. The obtained amorphous ordered mesoporous carbon was filtered, washed with ethanol and finally dried at 120 °C for 12 h.

2.3. Material characterization

The morphology of the AOMC and GNF was characterized using field emission scanning electron microscopy (FESEM, JEOL, JSM-6701F) and transmission electron microscopy (TEM, JEOL, JEM-2010). TEM was operated at an accelerating voltage of 200 kV, and equipped with an energy-dispersive X-ray (EDX) spectrometer (Bruker Quantax). Scanning transmission electron microscopy (STEM) analyses were carried out using a Hitachi HD2700C (200 kV). The structure was characterized by X-ray diffraction measurement (XRD, Rigaku, D/max-RB). The Raman spectra were performed on an iHR550 Raman microscope using a laser with excitation wavelength of 532 nm at room temperature. The surface area was measured according to the Brunauer-Emmett-Teller (BET) method.

2.4. Electrochemical measurements

The electrochemical performances were conducted using the CR2032 coin type half-cells. The electrode was ground and made into a slurry containing 80 wt% of the active material AOMC and 20 wt% of polyvinylidene fluoride (PVDF) in N-methylpyrrolidone. The mixture was thoroughly mixed and laminated onto a copper (for anode) or aluminium (for cathode) current collector and dried at 60 °C for 12 h under vacuum. Then a tablet machine was used to make a thin and smooth electrode slices. The diameter of every electrode slice is 14 mm and the thickness is about 50–100 μm. This electrode or GNF was used as the working electrode, and Na foil or sodium ion pre-intercalated SnO_2 electrode was used as both the counter and reference electrodes. The original SnO_2 with nanoscale is commercially purchased. The electrolyte used was a 1.0 mol L^{-1} $NaPF_6$ in a mixed solution of ethylene carbonate (EC) and dimethyl carbonate (DMC) with a volume ratio of 1:1 with 5% fluoroethylene carbonate (FEC). The glass fiber (GF/D) from Whatman was used as the separator. During the normal operation, the coin cells were assembled and disassembled in an argon-filled glovebox. The electrode was sealed in an argon-filled container and quickly taken out before the XRD and XPS measurements. Galvanostatic charge and discharge process was conducted using the LAND-CT2011A battery-testing instrument at room temperature under different current densities. Cyclic voltammetry (CV, CHI 660e) measurements were conducted with a scan rate of 0.1 mV s^{-1}.

3. Results and discussion

The schematic illustration of charge and discharge process of this new NDIBs system using AOMC cathode is shown in Fig. 1a–e. The discharge process is firstly carried out in the original battery, during which the Na ions remove from the Na metal anode, move through the electrolyte to the cathode and intercalate into the AMOC electrode (Fig. 1a). In the external circuit, the electrons transfer from the anode to cathode side. In the subsequent charge process, the Na ions deintercalate from the cathode and deposit onto the anode at low voltage (Fig. 1b). When charged at high voltage, the PF_6^- anions begin to intercalate into the AOMC electrode (Fig. 1c). And in the external circuit, the electrons transfer from the cathode to the anode side. In the following discharge process, the reversible reaction takes place, that is, the PF_6^- anions deintercalate from the cathode and move to the electrolyte at high voltage (Fig. 1d), and the Na ions remove from the anode and intercalate into the AMOC electrode at low voltage (Fig. 1e). Unlike the graphene cathode grown on the nickel foam (GNF) that can only accommodate the PF_6^- anions (Fig. S1 online), the AOMC cathode can accommodate two kinds of ions (Na ion and PF_6^- anions) due to its amorphous feature, hence contributing to a higher capacity.

The AOMC cathode was synthesized by a template method using sucrose as carbon source and SBA-15 as template. The lattice structure of AOMC was tested by wide and low-angle XRD. Two

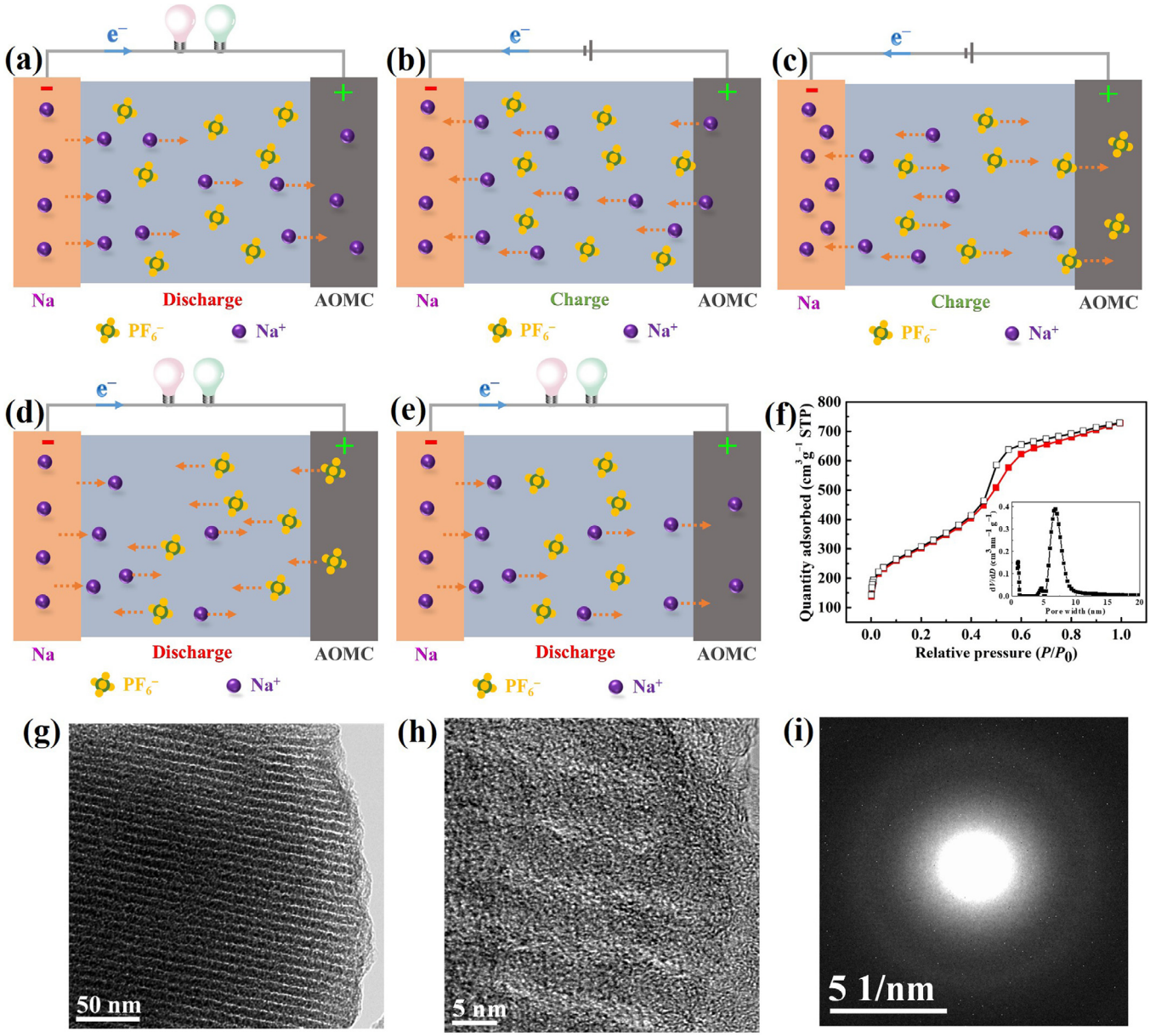

Fig. 1. (Color online) Schematic illustration of storage mechanism AOMC-based NDIBs and characterization of AOMC. (a–e) Schematic illustration of the charge and discharge process of AOMC-based NDIBs. (f) Nitrogen adsorption-desorption isotherms and pore size distribution (inset of f) of AOMC. (g) TEM, (h) HRTEM images and (i) the corresponding SAED pattern of AOMC.

broad peaks at approximately 23° and 44° are observed from the wide-angle XRD pattern (Fig. S2 online), indicating its amorphous phase. An intense peak and two weak peaks are observed from the low-angle XRD pattern, corresponding to the (1 0 0), (1 1 0) and (2 0 0) lattice planes, respectively, characteristic of two-dimensional (2D) hexagonally ordered pore arrangement [36]. The Raman spectrum of AOMC (Fig. S3 online) shows that the D-band (assigned to A_{1g} vibration mode of sp^2 carbon rings caused by defects) is more intensive than the G-band (assigned to E_{2g} vibration mode of sp^2 carbon atoms) with a I_D/I_G value of 1.25, indicating its low degree of graphitization. Fig. 1f shows the N_2 adsorption/desorption isotherm profile of the as-prepared AOMC. The type IV isotherms (IUPAC definition) are obtained with a high BET surface area of 1070 $m^2 g^{-1}$. The high nitrogen uptakes at the low relative pressure demonstrate the high microporosity of the as-prepared AOMC, while the H1 hysteresis loop reveals the presence of mesopores [37]. The average pore size is centered at 6.5 nm (inset of Fig. 1f), and meantime a small portion of pores peaked at 0.5 and 2.4 nm are observed, representing the existence of the micropores and mesopores. The typical SEM (Fig. S4 online) and TEM (Fig. 1e, 1f) images of the AOMC show the microflake structure with the diameter of 500 to 800 nm. When viewed along the direction of hexagonal pore arrangement, the as-prepared AOMC displays a well-ordered hexagonal arrangement of mesoporous channels, an inverse replica of SBA-15. The amorphous nature was further proved by the selected area electron diffraction (SAED, inset of Fig. 1f), well agreeing with the results from XRD patterns and Raman spectra. The graphene grown on the nickel foam was also synthesized (Figs. S5, S6 online). The differential scanning calorimetry-thermogravimetric analysis (DSC-TGA) was also carried out to measure the loading content of graphene in GNF (Fig. S7 online). The value is calculated to be 16.3%, being in good accordance with the results from elemental analyzer method (Table S1 online).

The GNF cathode was firstly tested in the coin cell. Fig. S8 (online) shows the galvanostatic charge and discharge profiles for NDIBs. Two high discharge voltage plateaus (4.6 and 4.1 V) and one charge plateau (4.7 V) are clearly observed (Fig. S8a online), being in accordance with the cyclic voltammograms (CV) curves (Fig. S9 online). The capacity tends to be stable after 10 cycles. The final capacity of GNF reaches 102 mAh g^{-1} over 50 cycles at 0.5 A g^{-1}, with a Coulombic efficiency of ca. 100% (Fig. S8b online). The energy dispersive X-ray spectrometry (EDS) mappings of the GNF electrode before and after a charge process (Fig. S10 online) show that only PF_6^- anions intercalate/deintercalate into/from the GNF cathode, being consistent with the previous reports [28,29]. Indeed, when evaluated as anode for SIBs, the carbon materials usually show low voltage plateau of ca. 0.3 V, indicating that the intercalation/deintercalation behavior of Na ions only happens at low voltage [38]. Therefore, in the high voltage range between 1.5 and 5.0 V, the Na ions do not participate in the intercalation/deintercalation process.

However, when the AOMC electrode was used as anode for SIBs, the charge and discharge curves are quite different. The voltage plateau is inconspicuous, and the intercalation/deintercalation behavior is observed in a wide voltage range (Fig. S11 online). The optical photograph of a charged NDIB is shown in Fig. 2a. The galvanostatic charge and discharge curves are shown in Fig. 2b. To get a clear observation, the first discharge curve is separated out (inset of Fig. 2b). The assembled battery shows an open-circuit voltage of around 2.5 V, and is firstly discharged to 1.5 V with a capacity of 58 mAh g^{-1}. In this process, Na ions intercalate into the AOMC electrode, forming sodium carbide, Na_xC. In the subsequent process, this electrode is charged to 5.0 V. The following discharge curves are quite different from the first one. The charge and discharge voltage range is set to be 1.5–5.0 V. The second

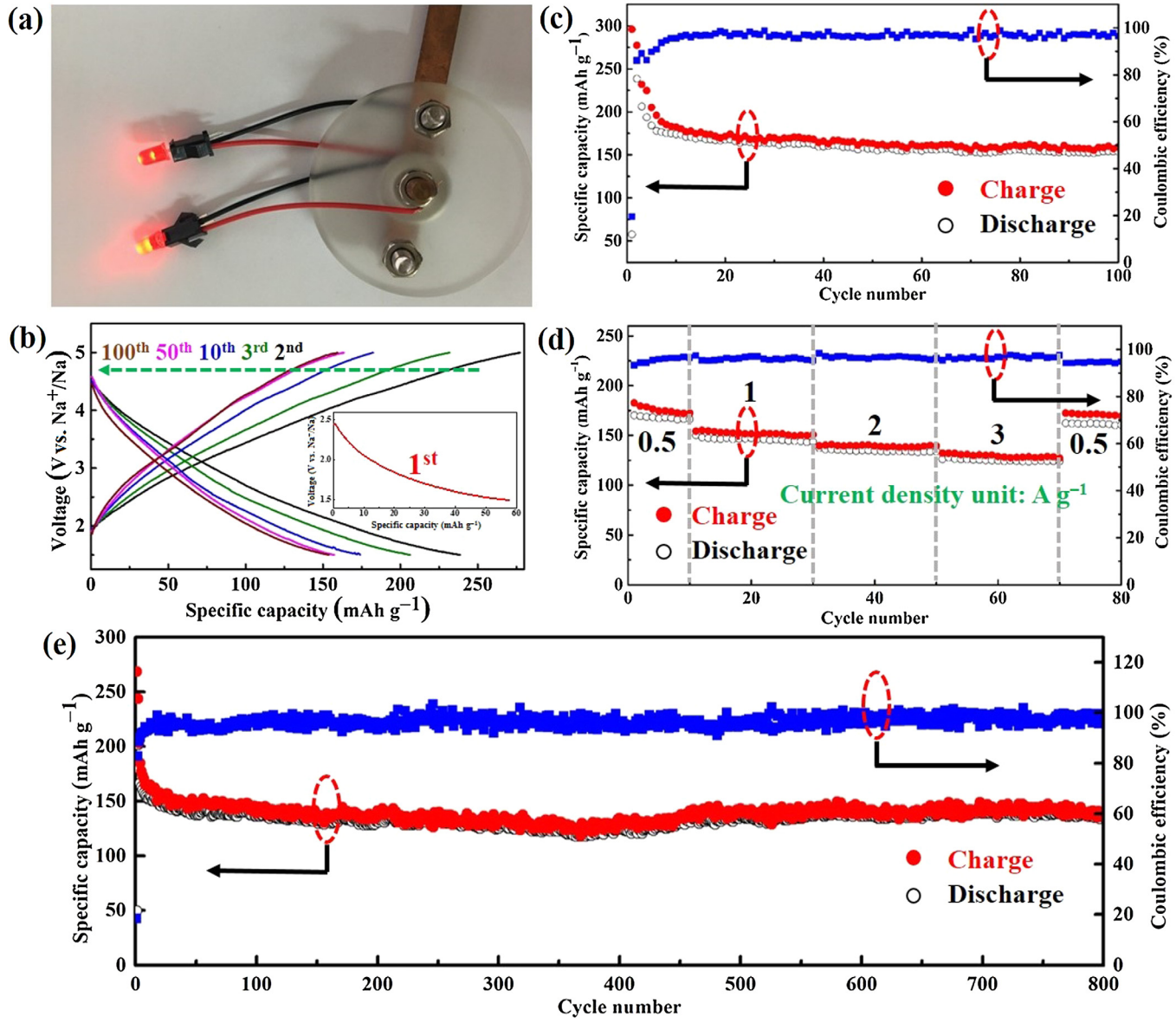

Fig. 2. (Color online) Electrochemical performance of AOMC–based NDIBs. (a) Optical photograph of the charged NDIBs. (b) The 2nd, 3rd, 10th, 50th and 100th charge and discharge curves of AOMC at 0.05 A g^{-1} for NDIBs. The inset of b shows the initial charge and discharge curves. (c) Charge and discharge capacity and Coulombic efficiency of AOMC at 0.05 A g^{-1}. (d) The rate performance from 0.5 to 3.0 A g^{-1} for NDIBs. (e) The cycle performance and Coulombic efficiency at a high current density of 2.0 A g^{-1} over 800 cycles.

charge and discharge capacities are 277 and 239 mAh g^{-1}, respectively, with a Coulombic efficiency of 86.3%. The capacity loss mainly occurs in the first ten cycles, attributable to the self-volume-accommodation process. The capacity loss after 10th cycle is much less, demonstrating a high reversibility, being in accordance with the CV curves (Fig. S12 online). To demonstrate the feasibility of this new-concept storage mechanism in full cell, we use sodium ion pre-intercalated SnO_2 as anode and AOMC as cathode to assemble the full cell (Fig. S13 online). The charge and discharge profiles are similar to those of half-cells, except for a lower voltage plateau. Over 100 cycles, the discharge capacity can remain as high as 127.8 mAh g^{-1} at a current density of 0.05 A g^{-1}.

The cycling stability and Coulombic efficiency of the AOMC at 0.05 A g^{-1} over 100 cycles are shown in Fig. 2c. In the first several cycles, although the capacity is a bit higher, yet the capacity loss is severer, and the Coulombic efficiency is low and unsteady, which may be due to the side reaction and self-volume-accommodation process. In the subsequent cycles, the amorphous carbon is transformed into partial graphitic stacking in a short range, thus forming a more stable structure. As a result, the Coulombic efficiency increases, and the capacity loss decreases. The capacity is more stable after 20 cycles, and can retain 159 mAh g^{-1} after 100 cycles with the capacity retention of approximately 93%, indicating good cycling stability. During charge process, the PF_6^- anions intercalate into the AOMC electrode, whereas during the subsequent discharge process, a small amount of PF_6^- anions are stuck and cannot deintercalate from the AOMC, resulting in the Coulombic efficiency below 100%.

The rate performance of the as-prepared AOMC at different current densities was also evaluated from 0.5 to 3.0 A g^{-1} for NDIBs (Fig. 2d). Reversible capacities of 172, 151, 139 and 127 mAh g^{-1} are observed after increasing the charge and discharge current densities to 0.5, 1.0, 2.0 and 3.0 A g^{-1}. Remarkably, after 70 cycles at different current densities, the capacity can be restored to 170 mAh g^{-1} when the current density returns to 0.5 A g^{-1}, indicating excellent rate performance and reversibility of NDIBs. The capacity comparison of AOMC and GNF at different current densities demonstrates that the rate performance of AOMC is much better than that of GNF (Fig. S14 online).

Long-term cycling stability at a high current density of 2.0 A g^{-1} over 800 cycles are presented in Fig. 2e. A reversible capacity of 136 mAh g^{-1} is obtained over such a long-time charge and discharge process with a capacity decay of only 0.02% per cycle. Such excellent capacity and cycling stability are superior to most of the reported NDIBs, even lithium-based DIBs (Tables S2, S3 online).

For better understanding the intercalation and deintercalation mechanism, X-ray photoelectron spectroscopy (XPS) was performed to investigate the chemical composition and the surface electronic state of the as-prepared AOMC (Fig. 3a–d). The C 1s spectra of the AOMC electrode at different charge and discharge states are shown in Fig. 3a. Typical C-C spectrum is observed in the original AOMC [39], while after the first discharge process (a1), this peak becomes weak. And at the same time the C-Na peak at 286.3 eV begins to appear [40], indicating the intercalation of Na ions. In the subsequent process charged to 2.5 and 3.5 V (a2 & a3), the C-C peak continues to disappear, and the C-Na peak is almost totally disappeared at 3.5 V. Meantime, two obvious peaks at 294.6 and 297.3 eV that appear at higher binding energy can be attributed to two types of C-F peaks, corresponding to the previous report of CHF_3 and CF_4 [41]. When charged to 5.0 V (a4), the intensity of the C-F peak becomes stronger, indicating the continuous intercalation of PF_6^- anions into the AOMC electrode. In the following discharge process (a5–a7), the intensities of the C-F peaks gradually become weak, accounting for the deintercalation of PF_6^-

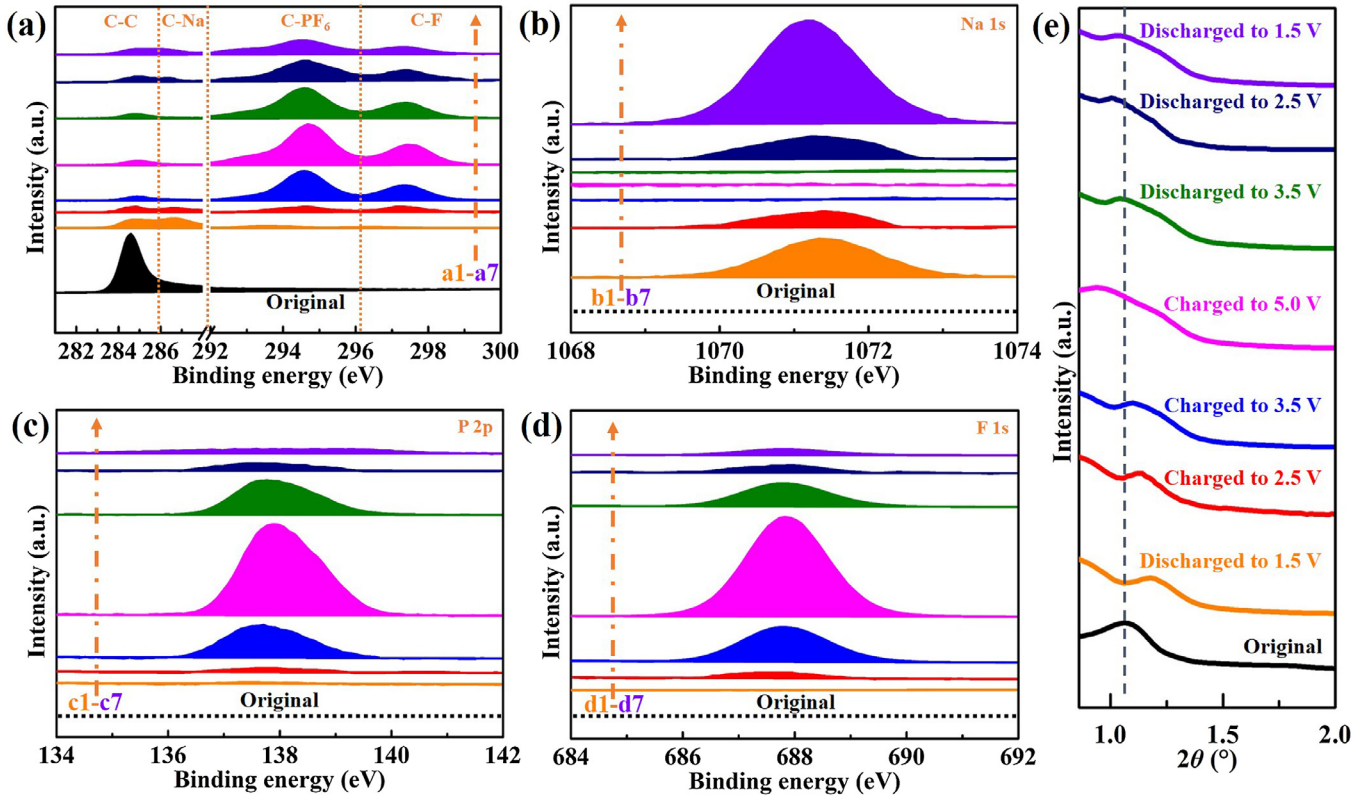

Fig. 3. (Color online) XPS spectra and *ex-situ* XRD patterns of different charge and discharge states. XPS spectra of the AOMC electrode at different charge and discharge states: (a) C, (b) Na, (c) P and (d) F. a1, b1, c1, d1: discharged to 1.5 V of the first cycle. a2, b2, c2, d2: charged to 2.5 V of the second cycle. a3, b3, c3, d3: charged to 3.5 V of the second cycle. a4, b4, c4, d4: charged to 5.0 V of the second cycle. a5, b5, c5, d5: discharged to 3.5 V of the second cycle. a6, b6, c6, d6: discharged to 2.5 V of the second cycle. a7, b7, c7, d7: discharged to 1.5 V of the second cycle. (e) *Ex-situ* low-angle XRD patterns of the AOMC electrode at different charge and discharge states.

anions. It should be noted that the intensity change of the C-Na peak only occurs between 1.5 and 3.5 V, indicating the Na ions intercalation and deintercalation only happen in this voltage range. The Na 1s spectra [42] of the AOMC electrode at different charge and discharge states (Fig. 3b) also show that the peak begins to appear when discharged to 2.5 V (b6), appears to be more obvious when discharged to 1.5 V (b1, b7), and disappears above 3.5 V (b3–b5), agreeing well with the result in Fig. 3a. This result demonstrates that the Na ions can intercalate into the AOMC only in a low voltage (<3.5 V). Usually it is difficult for the amorphous carbon to accmmodate Na ions in the voltage range of 1.5 to 3.5 V, while in this work the Na ions can intercalate/deintercalate into/from the AOMC. One reason can be attributed to the particular structure of partial graphitic stacking in short range, which has more ordered carbon atom arrangement than amorphous carbon and larger intercalayer spacing than graphite. This particular structure may affect the voltage during charge/dischage process. Another reason is that the intercalation/deintercaltion process is quite different from the common Na-ion batteries, as described in Fig. 1. The simultaneous intercalation/deintercalation of PF_6^- at the AMOC side in a charge or discharge process may increase the voltage for Na intercalation. The variation trends of P 2p and F 1s spectra at different charge and discharge states are quite similar (Fig. 3c, 3d). In the first discharge process to 1.5 V (c1, d1), no peaks can be observed. In the subsequent charge process from 1.5 to 5 V (c1–c4, d1–d4), both the P 2p and F 1s peak intensities gradually increase, indicating the intercalation of PF_6^- anions. Then the PF_6^- anions deintercalate from the AOMC in the following discharge process, along with the decrease of the P 2p and F 1s peak intensities (c4–c7, d4–d7) [43,44]. A slight peak shift can be also observed, which can be attributed to the different surrounding of the electron cloud. After more PF_6^- anions intercalated into the AOMC, the electron cloud around P and F atoms changed, leading to a slight change of binding energy. Only traces of the P 2p and F 1s peaks are left when discharged to 1.5 V, demonstrating the deintercalation of PF_6^- anions. After the full charge process in the second cycle, we also measured the element content of the AOMC cathode by disassembling the coin cell (Table S4 online). The atomic ratio of F to P is 6.23, close to that in PF_6^-, which demonstrates the intercalation of PF_6^- in cathode. In addition, the atomic ratio of C to P is 15.11, indicating the possible formation of $PF_6C_{15.11}$. The corresponding capacity of the intercalation of PF_6^- is ca. 147 mAh g^{-1}. Only a trace of Na element exists in the cathode, which means the majority of Na ions deintercalate from the cathode. Therefore, the deintercalation of Na in the second cycle contributes the same capacity as the initial discharge capacity, which is ca. 58 mAh g^{-1}. The adsorption behavior of PF_6^- on cathode can be another factor for the capacity contribution due to its large surface area [45]. Therefore, the total capacity of the charge process in the second cycle can be contributed by three parts, the intercalation of PF_6^-, the deintercalation of Na and the adsorption of PF_6^-. Based on the charge capacity of 277 mAh g^{-1} in the second cycle, the capacity contributed by the adsorption of PF_6^- is ca. 72 mAh g^{-1}.

The above data reveal that both Na ions and PF_6^- anions can intercalate/deintercalate into/from the AOMC electrode, well agreeing with the EDS mapping of the AOMC electrode during cycling (Fig. S15 online). The electrochemical reaction for the new NDIBs system is proposed as follows.

In the discharge process of the first cycle:

$$\text{Anode: } Na - e^- \rightarrow Na^+ \quad (1)$$

$$\text{Cathode: } xC + Na^+ + e^- \rightarrow NaC_x \quad (2)$$

$$\text{Overall: } Na + xC \rightarrow NaC_x \quad (3)$$

In the charge process of the second cycle:

$$\text{Anode: } Na^+ + e^- \rightarrow Na \quad (4)$$

$$\text{Cathode: } Na_xC - xe^- \rightarrow C + xNa^+ \quad (5)$$

$$C + yPF_6^- - ye^- \rightarrow C(PF_6)_y \quad (6)$$

In the discharge process of the second cycle:

$$\text{Anode: } Na - e^- \rightarrow Na^+ \quad (7)$$

$$\text{Cathode: } C(PF_6)_y + ye^- \rightarrow C + yPF_6^- \quad (8)$$

$$C + xNa^+ + xe^- \rightarrow Na_xC \quad (9)$$

$$\text{Overall: } (x - y)Na + yNaPF_6 + 2C \leftrightarrow Na_xC + C(PF_6)_y \quad (10)$$

Ex-situ low-angle XRD patterns of the AOMC electrode at different charge and discharge states were measured to further understand the electrochemical reaction (Fig. 3e). A distinct diffraction peak at 1.1°, attributed to the lattice plane (1 0 0), can be observed in the original AOMC, indicating the two-dimensional (2D) hexagonally ordered mesoporous arrangement [36]. When discharged to 1.5 V in the initial cycle, the diffraction peak shifts to a larger angle, indicating smaller mesopores. In the subsequent charge process, the Na ions deintercalate from the AOMC along with the intercalation of the PF_6^- anions into the AOMC. The combined result leads to the negative shift of the peak, indicating the increase of the carbon interlayer spacing. In the following discharge process, the peak can be partially recovered, demonstrating the recovery of the carbon interlayer spacing. These results show a high reversibility of the AOMC during charge and discharge process.

To study the formation of carbon layer and the variation of crystallinity, the Raman spectra of the AOMC at different charge and discharge states were performed (Fig. 4a–e). The degree of order in carbon materials was measured by the intensity ratio of D-band to G-band in the Raman spectra. When discharged to 1.5 V in the first cycle (Fig. 4a), the value of I_D/I_G decreases from 1.25 to 1.14, indicating a higher degree of graphitization. As the PF_6^- anions intercalate into the AOMC structure (Fig. 4b, c), the value of I_D/I_G continues to decrease. Even when the PF_6^- anions deintercalate from the AOMC, the value of I_D/I_G slightly recovers. This particular phenomenon can be explained as follows. The intercalation of Na cation or PF_6^- anion into the amorphous carbon can result in the rearrangement of carbon atoms and realize the transformation from the disordered carbon to the partial graphitic stacking in short range (Fig. 4f, section A and B). Although the PF_6^- anion deintercalates from the AOMC electrode in the discharge process of the second cycle, the value of I_D/I_G only slightly increases from 1.01 to 1.04 (Fig. 4f, section C), indicating almost same degree of order, which is due to the replacement of PF_6^- by Na^+ during the Na intercalation process. The Raman spectra of the GNF at different charge and discharge states are also carried out to demonstrate the degree of order (Fig. S16 online). The original GNF is well crystallized, and after a discharge process, the intensity of D-band becomes higher, indicating the emergence of more defects derived from the intercalation of Na ions. Meanwhile, the 2D-band splits into a few peaks, implying the aggregation of more graphene layers. And after the subsequent charge process, the D-band begins to appear, activated by the defect introduced from the intercalation of PF_6^- anions.

The intercalation and deintercalation mechanisms for graphite and AOMC are illustrated in Fig. 5. The interlayer spacing of graphite is 3.40 Å (Fig. S17a, d online). During a charge process, the PF_6^- anions are squeezed into the interlayer spacing (Fig. 5a). The graphite layers deform severely, and the interlayer spacing

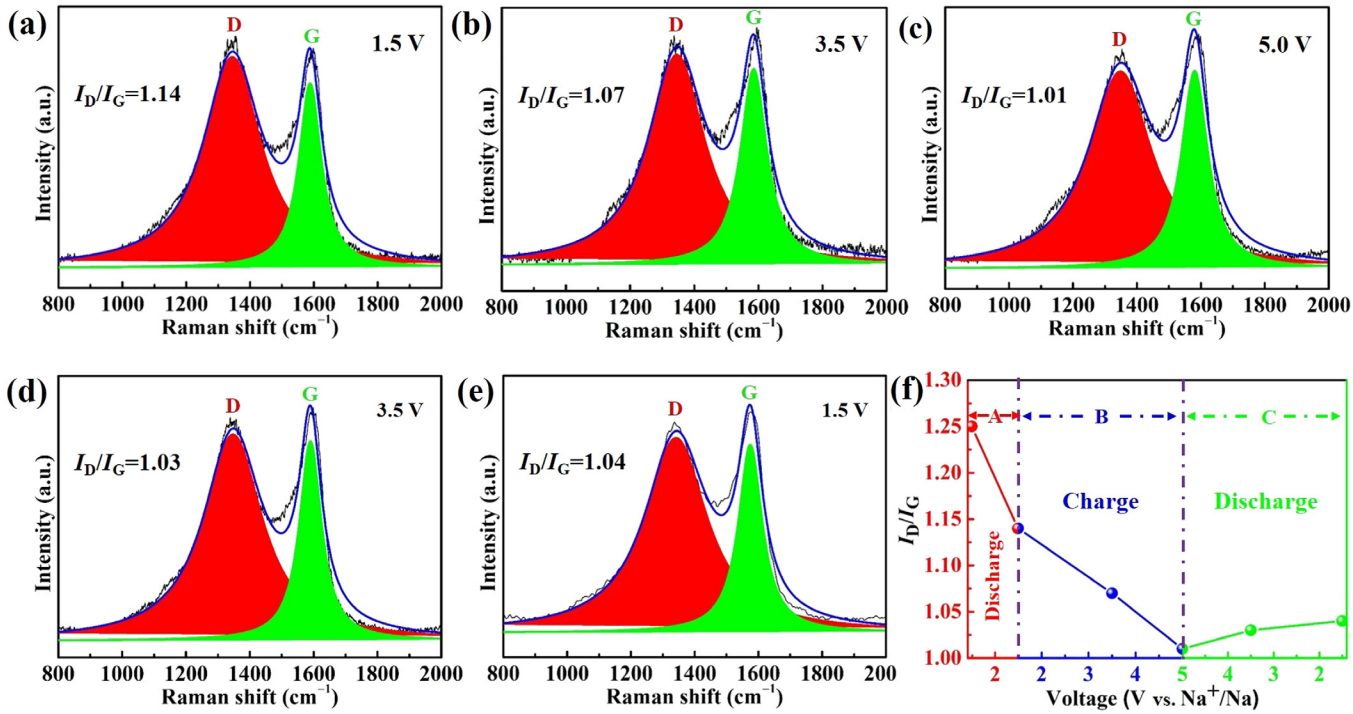

Fig. 4. (Color online) Raman spectra of different charge and discharge states. Raman spectra of the AOMC electrode at different charge and discharge states: (a) discharged to 1.5 V of the first cycle, (b) charged to 3.5 V of the second cycle, (c) charged to 5.0 V of the second cycle, (d) discharged to 3.5 V of the second cycle, (e) discharged to 1.5 V of the second cycle. The black line is the original curve, the blue line is the fitted curve, the red peak is the D band, and the green peak is the G band. (f) The relationship between the charge and discharge states and the intensity ratio of D-band to G-band.

increases up to 4.18 Å (Fig. S17b, e online). Even after the PF_6^- anions entirely deintercalate from the graphite layer, the interlayer spacing cannot recover to its original value (Fig. S17c, f online). The deformation of graphite layer can cause the structure collapse after the repeated cycles, resulting in a poor cycle life. The TEM image of GNF after 800 cycles (Fig. S18 online) shows that the morphology is largely changed, and the lattice fringe becomes unconspicuous, indicating the large deformation of graphite layer during cycling. The carbon atoms are disordered in amorphous AOMC, while after a discharge process (Stage I), Na ions intercalate into the AOMC, accompanying by the rearrangement of carbon atoms from disordered to partial graphitic stacking in a short range (Figs. 5b, S19a (online)). The lattice fringe can be seen, and the interlayer spacing is measured to be 3.74 Å (Fig. S19c online). In the subsequent charge process, the Na ions deintercalate from the NaC_x, and meantime the PF_6^- anions intercalate into the AOMC (Stage II). At the end of this process, the interlayer spacing further increases to 4.36 Å (Stage III, Fig. S19b, d online). This interlayer spacing is much larger than that of graphite, which can better accommodate the increased interlayer spacing and volume expan-

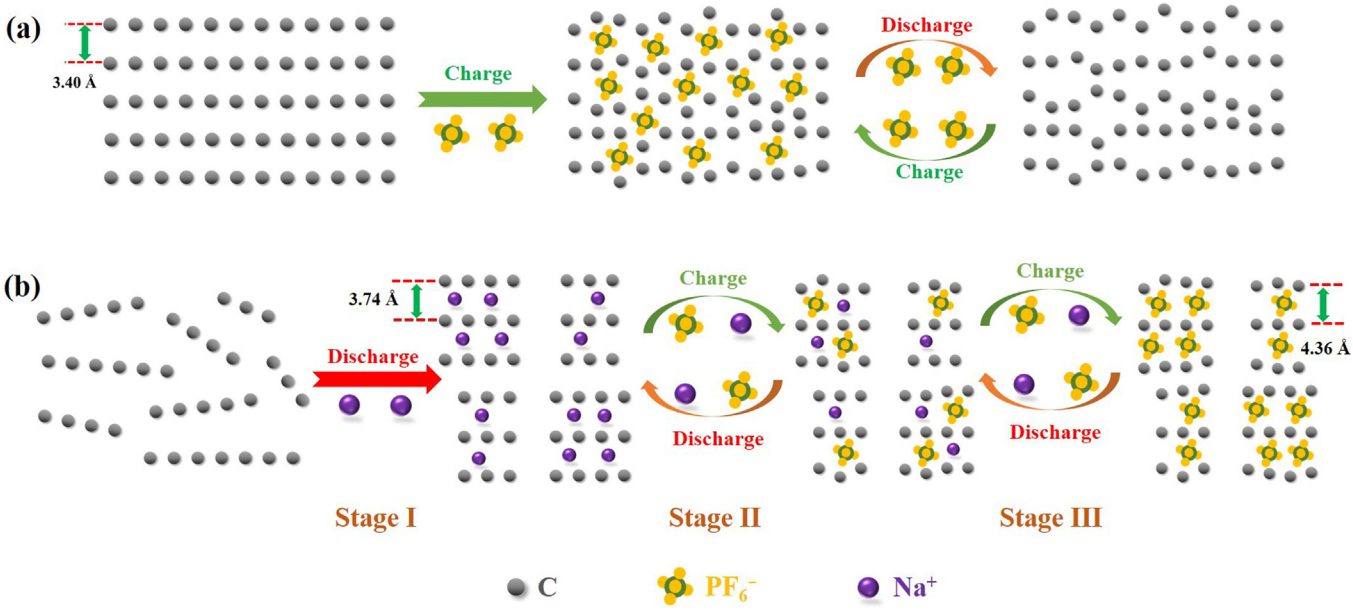

Fig. 5. (Color online) Schematic of storage mechanism for graphite and AOMC. Schematic illustration of the charge and discharge process of (a) graphite and (b) AOMC for NDIBs.

sion. This can be also proved by TEM images (Fig. S20 online), showing even after 800 cycles the morphology of AOMC is mainly maintained.

The reasons for the high-performance NDIBs are as follows: (1) The storage mechanisms of graphite and AOMC are quite different. In graphite, only PF_6^- anions can intercalate/deintercalate into/from the graphitic layers in the voltage range of 5.0–1.5 V, while both Na ions and PF_6^- anions can intercalate/deintercalate into/from the AOMC, enhancing the capacity performance. (2) Unlike the well-crystallized graphite, in which the PF_6^- anions are squeezed into the restricted interlayer spacing, resulting in low capacity and poor stability, we found that the amorphous AOMC has larger interlayer spacing in a short range, making it possible to accommodate more ions and tolerate the deformation of carbon layers.

4. Conclusion

In summary, we demonstrate a conceptually new NDIBs that both Na ions and PF_6^- anions can simultaneously intercalate/deintercalate into/from the AOMC electrode, totally different from the previous reported graphite-based dual-ion storage mechanism. During the charge and discharge processes, the disordered carbon in AOMC can be transformed to the partial graphitic stacking with large interlayer spacing and unique layered structure in short range after cycling. These features lead to a new NDIBs system with very high capacity, high rate performance and excellent stability. They deliver the charge and discharge capacities of 277 and 239 mAh g^{-1} at a current density of 0.05 A g^{-1}, respectively, much higher than the reported traditional graphite-based NDIBs. They can also retain a highly reversible storage capacity of 136 mAh g^{-1} for over 800 cycles at a very high current density of 2.0 A g^{-1}. Thus, the environmentally-friendly, cost-effective and high-energy-density AOMC electrode for NDIBs provides excellent guidance for the design of future multi-ion battery system and shows attractive potential for high-performance energy storage application.

Conflict of interest

The authors declare that they have no conflict of interest.

Acknowledgments

This work was supported by the National Key Research and Development Program of China (2016YFB0100201), the National Natural Science Foundation of China (51671003), the start-up supports from Peking University, Young Thousand Talented Program and National Innovation Zone of Defense Science and Technology of China (8205100116).

Author contributions

Wei (Alex) Wang and Shaojun Guo conceived the idea and designed the experiments. Wei (Alex) Wang, Hanxin Huang, Bin Wang and Zibin Liang performed the characterization and analyzed the data. Chang Qian, Peihao Li, Jinhui Zhou and Chao Yang performed the electrochemical test.

Appendix A. Supplementary data

Supplementary data to this article can be found online at https://doi.org/10.1016/j.scib.2019.08.021.

References

[1] Gao X, Chen Y, Johnson L, et al. Promoting solution phase discharge in Li-O_2 batteries containing weakly solvating electrolyte solutions. Nat Mater 2016;15:882–8.
[2] Wang W, Lv F, Lei B, et al. Tuning nanowires and nanotubes for efficient fuel-cell electrocatalysis. Adv Mater 2016;28:10117–41.
[3] Wang H, Wang M, Tang Y. A novel zinc-ion hybrid supercapacitor for long-life and low-cost energy storage applications. Energy Storage Mater 2018;13:1–7.
[4] Wu H, Zheng G, Liu N, et al. Engineering empty space between Si nanoparticles for lithium-ion battery anodes. Nano Lett 2012;12:904–9.
[5] Dunn B, Kamath H, Tarascon JM. Electrical energy storage for the grid: a battery of choices. Science 2011;334:928–35.
[6] Bruce PG, Scrosati B, Tarascon JM. Nanomaterials for rechargeable lithium batteries. Angew Chem Int Ed 2008;47:2930–46.
[7] Tang Y, Zhang Y, Deng J, et al. Mechanical force-driven growth of elongated bending TiO_2-based nanotubular materials for ultrafast rechargeable lithium ion batteries. Adv Mater 2014;26:6111–8.
[8] Wang S, Xia L, Yu L, et al. Free-standing nitrogen-doped carbon nanofiber films: integrated electrodes for sodium-ion batteries with ultralong cycle life and superior rate capability. Adv Energy Mater 2016;6:1502217–24.
[9] Yabuuchi N, Kubota K, Dahbi M, et al. Research development on sodium-ion batteries. Chem Rev 2014;114:11636–82.
[10] Guo S, Li Q, Liu P, et al. Environmentally stable interface of layered oxide cathodes for sodium-ion batteries. Nat Commun 2017;8:135.
[11] Dong Y, Wu ZS, Zheng S, et al. Ti_3C_2 MXene-derived sodium/potassium titanate nanoribbons for high-performance sodium/potassium ion batteries with enhanced capacities. ACS Nano 2017;11:4792–800.
[12] Eftekhari A, Jian Z, Ji X. Potassium secondary batteries. ACS Appl Mater Inter 2016;9:4404–19.
[13] Zhang W, Mao J, Li S, et al. Phosphorus-based alloy materials for advanced potassium-ion battery anode. J Am Chem Soc 2017;139:3316–9.
[14] Choudhury S, Wan CTC, Sadat WIA, et al. Designer interphases for the lithium-oxygen electrochemical cell. Sci Adv 2017;3:1602809.
[15] Lu J, Lee YJ, Luo X, et al. A lithium-oxygen battery based on lithium superoxide. Nature 2016;529:377–82.
[16] Zhang X, Tang Y, Zhang F, et al. A novel aluminum-graphite dual-ion battery. Adv Energy Mater 2016;6:1502588.
[17] Read JA, Cresce AV, Ervin MH, et al. Dual-graphite chemistry enabled by a high voltage electrolyte. Energy Environ Sci 2014;7:617–20.
[18] Shi X, Zhang W, Wang J, et al. $(EMIm)^+(PF_6)^-$ ionic liquid unlocks optimum energy/power density for architecture of nanocarbon-based dual-ion battery. Adv Energy Mater 2016;6:1601378.
[19] Kundu D, Talaie E, Duffort V, et al. The emerging chemistry of sodium ion batteries for electrochemical energy storage. Angew Chem Int Ed 2015;54:3431–48.
[20] Slater MD, Kim D, Lee E, et al. Sodium-ion batteries. Adv Funct Mater 2013;23:947–58.
[21] Kim H, Yoon G, Park I, et al. Anomalous Jahn-Teller behavior in a manganese-based mixed-phosphate cathode for sodium ion batteries. Energy Environ Sci 2015;8:3325–35.
[22] Wang M, Tang Y. A review on the features and progress of dual-ion batteries. Adv Energy Mater 2018;8:1703320.
[23] Zhang M, Song X, Ou X, et al. Rechargeable batteries based on anion intercalation graphite cathodes. Energy Storage Mater 2019;16:65–84.
[24] Han P, Han X, Yao J, et al. Mesocarbon microbead based dual-carbon batteries towards low cost energy storage devices. J Power Sources 2018;393:145–51.
[25] Rodríguez-Pérez IA, Jian Z, Waldenmaier PK, et al. A hydrocarbon cathode for dual-ion batteries. ACS Energy Lett 2016;1:719–23.
[26] Deunf E, Jiménez P, Guyomard D, et al. A dual-ion battery using diamino-rubicene as anion-inserting positive electrode material. Electrochem Commun 2016;72:64–8.
[27] Deunf E, Moreau P, Quarez E, et al. Reversible anion intercalation in a layered aromatic amine: a high-voltage host structure for organic batteries. J Mater Chem A 2016;4:6131–9.
[28] Sheng M, Zhang F, Ji B, et al. A novel tin-graphite dual-ion battery based on sodium-ion electrolyte with high energy density. Adv Energy Mater 2017;7:1601963.
[29] Fan L, Liu Q, Chen S, et al. Soft carbon as anode for high-performance sodium-based dual ion full battery. Adv Energy Mater 2017;7:1602778.
[30] Liao HJ, Chen YM, Kao YT, et al. Freestanding cathode electrode design for high-performance sodium dual-ion battery. J Phys Chem C 2017;121:24463–9.
[31] Wang X, Zheng C, Qi L, et al. Carbon derived from pine needles as a Na^+-storage electrode material in dual-ion batteries. Global Challenges 2017;1:1700055.
[32] Reina A, Jia X, Ho J, et al. Large area, few-layer graphene films on arbitrary substrates by chemical vapor deposition. Nano Lett 2008;9:30–5.
[33] Losurdo M, Giangregorio MM, Capezzuto P, et al. Graphene CVD growth on copper and nickel: role of hydrogen in kinetics and structure. Phys Chem Chem Phys 2011;13:20836–43.
[34] Zhao D, Feng J, Huo Q, et al. Triblock copolymer syntheses of mesoporous silica with periodic 50 to 300 angstrom pores. Science 1998;279:548–52.
[35] Zhao D, Huo Q, Feng J, et al. Nonionic triblock and star diblock copolymer and oligomeric surfactant syntheses of highly ordered, hydrothermally stable, mesoporous silica structures. J Am Chem Soc 1998;120:6024–36.
[36] Shilapuram V, Ozalp N, Oschatz M, et al. Hydrogen production from catalytic decomposition of methane over ordered mesoporous carbons (CMK-3) and carbide-derived carbon (DUT-19). Carbon 2014;67:377–89.
[37] Reichhardt N, Kjellman T, Sakeye M, et al. Removal of Intrawall pores in SBA-15 by selective modification. Chem Mater 2011;23:3400–3.
[38] Kim SW, Seo DH, Ma X, et al. Electrode materials for rechargeable sodium-ion batteries: potential alternatives to current lithium-ion batteries. Adv Energy Mater 2012;2:710–21.

[39] Xie Y, Sherwood PM. Ultrahigh purity graphite electrode by core level and valence band XPS. Surf Sci Spectra 1992;1:367–72.
[40] Vannerberg N. Esca-spectra of sodium and potassium cyanide and of sodium and potassium-salts of hexacyanometallates of 1st transition-metal series. Chem Scripta 1976;9:122–6.
[41] Gelius U, Heden P, Hedman J, et al. Molecular spectroscopy by means of ESCA III. Carbon compounds. Phys Scripta 1970;2:70–80.
[42] Siriwardane RV, Cook JM. Interactions of NO and SO_2 with iron deposited on silica. J Colloid Interf Sci 1985;104:250–7.
[43] Klimov VD, Vashman AA, Pronin IS. Study of atomic titanium interaction with PF3 matrix at 77-K-cryochemical synthesis of TiF2. PF3 monotriphosphinetitanium (II) fluoride new compounds. Zh Obshch Khim 1991;61:2166–74.
[44] Van Attekum PTM, Van der Velden J, Trooster J. X-ray photoelectron spectroscopy study of gold cluster and gold(I) phosphine compounds. J Inorg Chem 1980;19:701–4.
[45] Yuan Y, Wang C, Lei K, et al. Sodium-ion hybrid capacitor of high power and energy density. ACS Cent Sci 2018;4:1261–5.

Wei (Alex) Wang is currently a postdoctoral researcher at Harvard University. In 2016, he received his Ph.D. degree in Metallurgical Engineering from University of Science and Technology Beijing. Then he worked at Peking University during 2016–2018 as a postdoctoral researcher. His research interests include the design, synthesis and characterization of advanced energy materials for Li/Na/K/Al-ion batteries, solid-state electrolyte and catalysis.

Shaojun Guo received his B.Sc. degree in Chemistry from Jilin University (2005), Ph.D. degree from Chinese Academy of Sciences (2010), worked as a postdoctoral research associate at Brown University (2011–2013) and as a prestigious Oppenheimer Distinguished Fellow at Los Alamos National Laboratory (2013–2015). In 2015, he joined at College of Engineering, Peking University. His current research interests focus on materials chemistry for catalysis, battery and sensor applications.